Energy Storage Materials 42 (2021) 286–294

Contents lists available at ScienceDirect

Energy Storage Materials

journal homepage: www.elsevier.com/locate/ensm

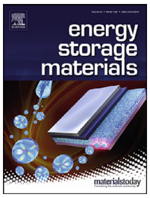

Spontaneous knitting behavior of 6.7-nm thin $(NH_4)_{0.38}V_2O_5$ nano- ribbons for binder-free zinc-ion batteries

Yingchang Jiang[a], Zeyi Wu[d], Fei Ye[b], Ruilvjing Pang[b], Lin Zhang[d], Qiang Liu[b], Xueting Chang[a], Shibin Sun[c,*], Zhengming Sun[b], Linfeng Hu[b,d,*]

[a] Institute of Marine Materials Science and Engineering, College of Ocean Science and Engineering, Shanghai Maritime University, Shanghai 201306, P. R. China
[b] School of Materials Science and Engineering, Southeast University, Nanjing, 211189, P. R. China
[c] College of Logistics Engineering, Shanghai Maritime University, Shanghai 201306, P. R. China
[d] Department of Materials Science, Fudan University, Shanghai 200433, P. R. China

ARTICLE INFO

Keywords:
$(NH_4)_{0.38}V_2O_5$
Ultrathin nanoribbons
Spontaneous knitting behavior
Binder-free cathode
Zinc ion batteries

ABSTRACT

Rechargeable, aqueous Zn-ion batteries in a neutral or mildly acidic electrolyte have attracted great attention. The fabrication of binder-free electrodes to boost the Zn^{2+} transport is extremely desirable for the development of aqueous zinc-ion batteries but remains a big challenge. Herein, we revealed a spontaneous knitting behaviour in 6.7 nm thin, flexible $(NH_4)_{0.38}V_2O_5$ nanoribbons by a hydrothermal route to form binder-free paper cathode for aqueous zinc-ion batteries. Conductive multi-walled carbon nanotubes (CNTs) was also successfully imbedded into this paper to enhance the electronic conductivity and produce abundant meshes (pore size: 1-3 μm) inside the paper. Taking advantage of the binder-free design and the porous architecture of the paper cathode, it delivered a reversible capacities of 465 $mAh{\cdot}g^{-1}$ at 100 $mA{\cdot}g^{-1}$. A capacity retention of above 89.3 % after 500 cycles at 100 $mA{\cdot}g^{-1}$ has been achieved. Importantly, the resulting paper electrode exhibited a specific energy as high as 343 $Wh{\cdot}kg^{-1}$, which remarkably outperforms most of the zinc-ion batteries based on powder form cathode with the presence of polymer binder. Our work reveals a novel self-grown strategy for the binder-free, freestanding electrodes on Zn^{2+} ion storage from the ultrathin, flexible ammonium vanadates nanostructures, and it might be applicable to the storage of other metal/non-metallic ions (Na^+, Mg^{2+}, Ca^{2+}, Al^{3+}, $NH_4{}^+$ etc.) in next-generation electrochemical energy storage devices.

1. Introduction

Rechargeable aqueous batteries are very promising owing to their low-cost, high safety and environmentally friendly feature as compared to the organic-based one [1,2]. Among various aqueous batteries, zinc-ion batteries (ZIBs) has been considered as one of the most popular energy storage devices. Remarkably, aqueous zinc-ion batteries (ZIBs) deliver the prominent superiority of relatively resource sustainability (abundant zinc resource reserve), better safety and environment friendly (aqueous-based electrolyte), excellent volumetric energy density (nearly 5855 $mAh{\cdot}cm^{-3}$ compared to 2061 $mAh{\cdot}cm^{-3}$ for lithium ion batteries) [3–8]. The development of aqueous ZIBs still faces key challenges related to the design of advanced cathode materials to match high-capacity Zn anodes. Up to date, the main cathode materials for ZIBs are Prussian blue analogues, [9–12] manganese oxides, [13–20] vanadium-based compounds, [21–28] quinone analogues [29–31]. In general, the active materials in ZIB cathode are prepared in powder form and the addition of polymeric binders (PVDF) are inevitable during electrode preparation [32–36]. Note that the presence of polymer binder severely blocks the transport of metal-ions at the current collector/active material interface. Especially, the Zn^{2+} diameter is close to that of Li^+ and thus the charge density of Zn^{2+} is much higher than Li^+, which induces a polarizing effect during the diffusion/transport process. Consequently, Zn^{2+} tends to be adsorbed to the C–F bonds in the polarizing PVDF binder and the mobility of Zn^{2+} significantly decreases, leading to poor rate-capacity, cycling stability and limited energy density of the as-assembled ZIBs [37]. In this respect, the fabrication of binder-free electrodes to avoid the sluggish Zn^{2+} transport kinetics in polymer binder is extremely desirable.

Some bottom-up approaches have been proposed to achieve this design recently. One strategy is to in-situ grow active compounds on some conductive substrates (such as nick foam, carbon clothes, etc.) [38–42]. Unfortunately, the in-situ growth strategy usually suffers from a low mass-loading and non-uniform distribution of the active materials on the

---

* Corresponding authors.
E-mail addresses: sunshibin@shmtu.edu.cn (S. Sun), linfenghu@seu.edu.cn (L. Hu).

https://doi.org/10.1016/j.ensm.2021.07.045
Received 3 June 2021; Received in revised form 21 July 2021; Accepted 28 July 2021
Available online 31 July 2021
2405-8297/© 2021 Elsevier B.V. All rights reserved.

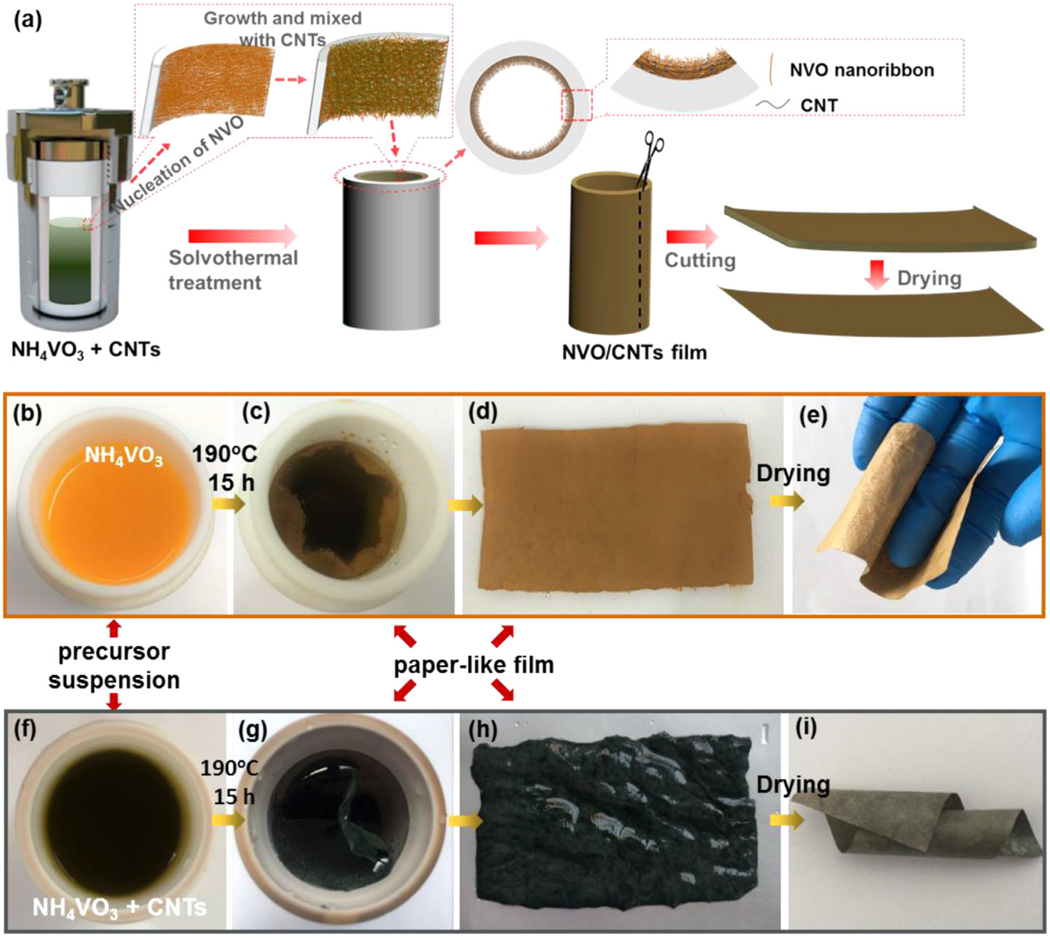

Fig. 1. (a) Schematic illustration of the spontaneous knitting process of ultrathin NVO nanoribbons/CNTs. Digital photographs of (b) the precursor suspension, (c, d) the self-knitted NVO membrane adhered to autoclave wall. (e) The NVO paper-like sample with a yellow color after drying. The digital photographs of (f) the precursor suspension with CNTs addition, (g, h) the NVO /CNTs membrane adhered to autoclave wall, and (i) the black, flexible NVO /CNTs paper after drying.

current collector, resulting in unsatisfied battery performance on energy density and cycling stability. Another important strategy is to construct artificial, freestanding membrane from mono-dispersed nano-building blocks through a vacuum filtration strategy. However, such a process is very time-consuming, and the thin-membrane fabricated by this approach cannot easily be peeled off from the filter membrane. The fracture of membrane during the peel-off process leads to some fragments with a limited size, which is generally unstable in liquid electrolyte and remarkably hinders its battery applications [43–45]. Hence, it would be quite ideal if a bind-free cathode can be grown directly during the preparation process. However, to the best of our knowledge, such a proposal has never been realized and remains a challenge.

Herein, we accidentally found an interesting, spontaneous knitting behaviour in 6.7 nm thin $(NH_4)_{0.38}V_2O_5$ (NVO) nanoribbons by a hydrothermal route, resulting in a freestanding membrane adhered to hydrothermal autoclave wall. Such a membrane was easily transfered from the autoclave wall into glass garden by a pair of tweezers to be a binder-free, freestanding paper sample (Fig. 1). Conductive multi-walled carbon nanotubes (CNTs) was also successfully imbedded into this paper to enhance the electronic conductivity and produce abundant meshes. Optimized by the incorporation of conductive multi-walled carbon nanotubes (CNTs) into this paper, the resulting $(NH_4)_{0.38}V_2O_5$/CNTs (NVO/CNTs) hybrid paper delivered a very high reversible capacities of 465 mAh·g^{-1} at 100 mA·g^{-1}, and a capacity retention of above 89.3% after 500 cycles at 100 mA·g^{-1} when used a ZIB cathode. The energy density of the as-constructed battery was as high as 343 Wh·kg^{-1}, which remarkably outperformed most of the zinc-ion batteries based on powder form cathode with the presence of polymer binder. We further realized quasi-solid-state ZIBs from the self-knitted NVO/CNTs membrane with excellent flexibility and mechanical stability.

2. Results And Discussion

We started our work by preparing a homogeneous aqueous suspension from the commercial NH_4VO_3 power with the controllable adjustment of pH value to 6.0 by dropping hydrochloric acid (HCl, 2M) slowly with continuous stirring. After 190°C hydrothermal treatment of the aforementioned aqueous suspension, an orange colored membrane can be observed in the autoclave continuously curved along the inner wall. Such a membrane can be easily transferred from the autoclave into glass garden by a pair of tweezers. After washing server times by deionized water and ethanol, the self-grown film was dried at 60°C overnight with a significant shrinkage in thickness (before drying: 2-3 mm, after drying: 20-30 microns, as shown in Fig. 1 b-i), which makes them similar to paper-like sample on the morphology and texture. We found a hydrothermal temperature of 190°C is essential to form such a paper-like sample with a high purity. Lower temperature less than this value gives rise to some white precipitation on the surface of paper-like sample, whcih cannot be removed by repeated water/ethanol washing (Fig. S1).

Fig. 2a shows X-ray diffracyion (XRD) data of the as-grown paper-like sample. Most of the diffraction peaks well match the monoclinic $(NH_4)_{0.38}V_2O_5$ (JCPDS No. 27-1019). Very sharp (00l) (l = 1, 3) diffraction peaks were detected with much higher intensity than other peaks, indicating the as-grown NVO is highly crystallized with

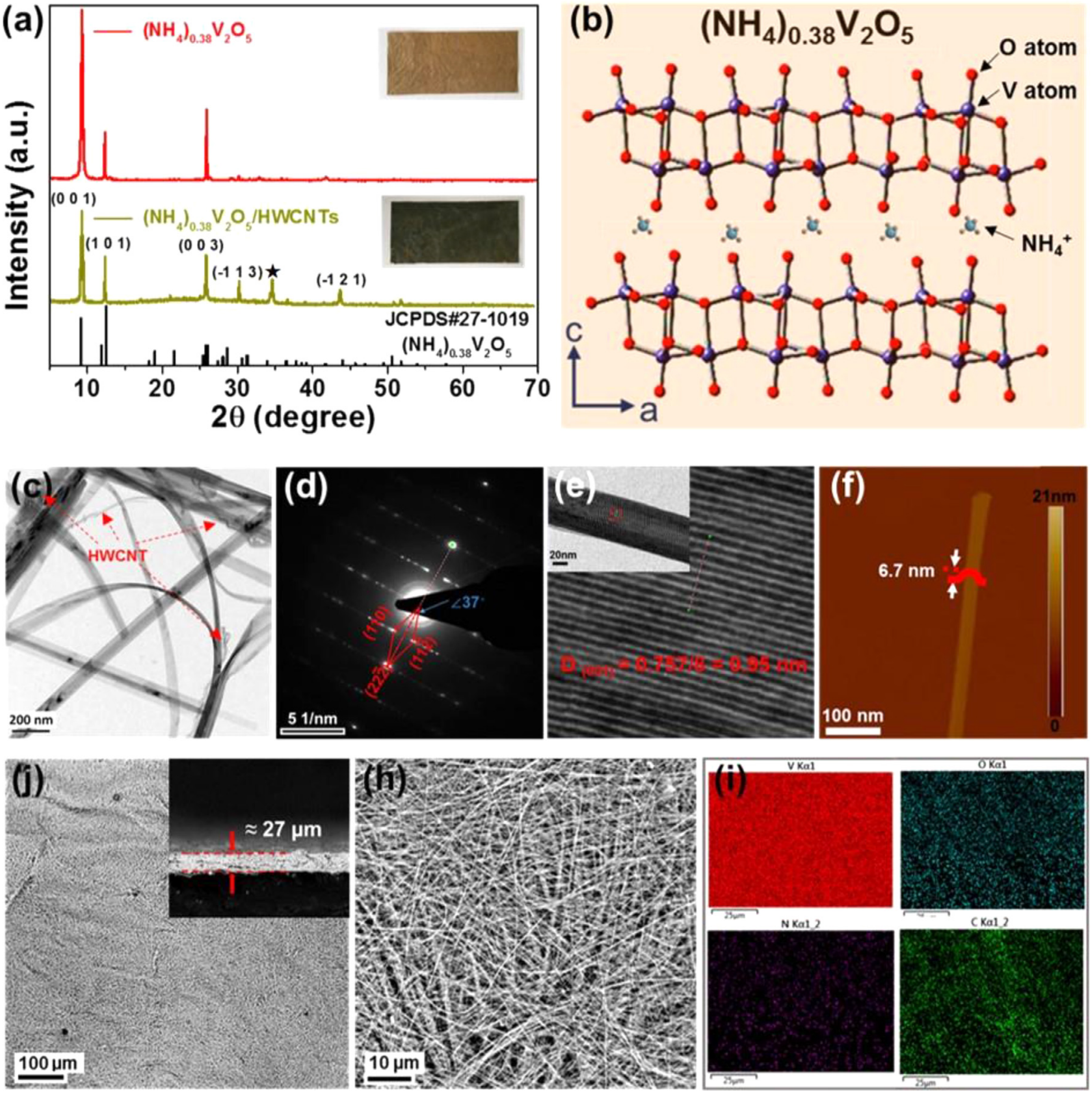

Fig. 2. (a) XRD patterns of pristine NVO paper and NVO/CNTs composited paper (inset is the corresponding photograph, respectively). The additional peak at $2\theta = 24.5^{\circ}$ is due to the CNT diffraction peak, and the peak at $2\theta = 34.6^{\circ}$ may contibute from some impurity. (b) The atomic structure of layered NVO crystal. (c) Typical TEM image of NVO/CNTs hybrids. (d) SAED pattern and (e) HRTEM image of NVO nanoribbons. (f) AFM image of an individual nanoribbon. (j, h) SEM images of NVO/CNTs hybrid film. Inset is the corresponding cross-section SEM image showing the thickness. (i) EDS elemental mappings for V, O, N and C elements in the NVO/CNTs composite film, respectively.

a preferred [001] orientation. As shown in Fig. 2b, the monoclinic NVO unit cell is consisted of distorted, edge-sharing VO_6 octahedron to form a stable bi-layered structure. The single-connected oxygen atoms in the octahedron generate strong interactions with intercalated ammonium ions. The ammonium ions are inclined to serve as "pillar" cations to stabilize the structure against volumetric changes during the insertion/de-insertion processes of guest ions at the interlayer spacing. Note that the (001) interlayer spacing of NVO is estimated as 9.67 Å, which is much larger than those of the previously reported $NH_4V_3O_8{\cdot}1.9H_2O$, [46] $NH_4V_4O_{10}$, [47] $K_{0.5}V_2O_5{\cdot}0.76H_2O$, [48] $Na_2V_6O_{16}{\cdot}3H_2O$, [49] $Ca_{0.25}V_2O_5{\cdot}nH_2O$, [50] zinc pyrovanadate [51]. Such a large interlayer spacing triggered from intercalated ammonium ions would be beneficial for the Zn^{2+} insertion and diffusion, which is generally critical to the improvement of electrochemical performance on specific capacity and rate capability [52,53].

Considered that ammonium vanadates generally suffer from low electronic conductivity which significantly hinders the electron transport when it was used as battery electrode, we tried to incorporate conductive multi-walled carbon nanotubes (CNTs) into this paper-like sample. The negatively charged surface of both aqueous suspension of NH_4VO_3 and carbon nanotube was determined by Zeta potential measurement (Fig. S2). Thus, a stable colloidal suspension was readily obtained through homogeneously mixing commercial NH_4VO_3 aqueous suspension and CNTs suspension followed by an ultrasonic treatment with an optimized mass ratio of 8:1 (NVO: CNTs). After the hydrothermal treatment under the same condition, a self-grown membrane along the autoclave inner wall can be also observed. The color of this membrane changes into brown and seems very uniform, suggesting the successful incorporation of carbon nanotubes inside the membrane. Many strong diffraction peaks appear in the XRD pattern of NVO/CNTs compared to the resulted pure NVO. It should be noteworthy that most of these emerging diffraction peaks can also be indexed into $(NH_4)_{0.38}V_2O_5$ phase (such as (-113), (-121) plane, etc.). In general, a highly [001] oriented sample just show (00*l*) (l = 1, 2, 3…) diffraction peaks with a much higher intensity compared with the isotropic sample. Accordingly, the appearance of other diffraction peaks suggests the embedding of CNTs slightly decreases the arrangement orientation of the NVO nanoribbons. Such a suppose is also confirmed by the distinct change on the peak intensity ratios of various diffraction peaks to the (001) peak after the incorporation of CNTs.

The morphology and chemical composition were checked by transmission electron microscopy (TEM) and scanning electron microscope (SEM) characterizations. TEM observation of the sample by an ultrasonic treatment of the NVO/CNTs paper in ethanol solvent is shown in Fig. 2c-e. The result demonstrates the presence of long NVO nanoribbons inside the paper-like sample with a length of several ten microns and diameters of 200−500 nm. The random bending state of these NVO nanoribbons suggests its inherent flexibility, leading to the spontaneous knitting behavior as discussed below. We can also observe the carbon nanotubes which are cross-linked with the bent NVO nanoribbons in Fig. 2c. The corresponding selected area electron diffraction (SAED) pattern taken from an individual NVO nanoribbon displays a single-crystal pattern with rectangular arrangement of sharp diffraction spots (Fig. 2d). The representative high-resolution TEM (HRTEM) images in Fig. 2e also indicates the high crystallinity nature, and a well resolved 9.5 Å spacing of the lattice fringes agreeing well with the expected separation of (001) planes, respectively (Fig. 1d). Note that the nanoribbons are almost semi-transparent under TEM observation, indicating e-beam can penetrate the sample due to their ultrathin thickness. In addition, the thickness of an individual nanoribbon was accurately examined to be ~6.7 nm by tapping-mode atomic force microscopy (AFM) characterization (Fig. 2f). Fig. 2j, 2h and Fig. S3 display typical SEM morphology of pristine NVO and NVO/CNTs composited paper, respectively. SEM observation confirms that NVO nanoribbons and CNTs are randomly connected with each other and self-assembled into continuous and interconnected three-dimensional (3D) network with abundant meshes (pore size: 1-3 μm). Such a porous structure would remarkably facilitate the penetration of liquid electrolyte, which ensures excellent ionic contact together with the facilitated fast electron/ion transport. The uniform distribution of CNTs in the NVO/CNTs paper has been further confirmed by the EDS analysis as shown in Fig. 2i, which effectively inhibits the aggregation of NVO nanoribbons and facilitate the electron transfer used electrode for battery application. As a comparison, the TEM, SAED and EDS characterization of pure NVO paper was also performed (Fig. S4 and S5). It is clear that the embedding of CNTs in this paper almost had no influence on the NVO nanoribbon morphology. The cross-section SEM image in Fig. S6 suggests the thickness of this composited paper can be easily regulated from 20 to 285 μm by changing the concentration of precursor solution. The density of the 65 μm thick NVO/CNTs paper is 1.63 mg·cm^{-2}, which is slightly larger than 1.49 mg·cm^{-2} of common paper napkins with the thickness of 78 μm. The mechanical tests of above resulted papers were performed using a WDW-0.1 electronic universal testing machine (Shanghai Bairoe Test Instrument Co., Ltd). Seen from the result in the Fig. S7, the tensile strength of our 65 μm thick NVO/CNTs paper is 0.38 MPa, reaches 70% of commercial paper counterpart. The resistivity of these paper-like samples measured by a four-probe tester are 0.02 mΩ·cm^{-1} and 6320 mΩ·cm^{-1} for NVO/CNTs composite and pure NVO, respectively, demonstrating the great enhancement on electronic conductivity of the as-grown paper by carbon nanotubes introduction.

Although the real formation mechanism of such a paper sample formed on the autoclave inner wall is still not very clear yet, we consider that the main reason should be attributed to the intrinsic flexibility of our very long NVO nanoribbons with a length of several ten microns and diameters of 200−500 nm. Such a highly flexible one-dimensional nanostructures are easily rolled up and spontaneously knitted into a paper. Such a phenomenon is a little similar to the Chinese paper found about 2000 years ago, which were also fabricated from long, natural vegetable fibers. In our case, firstly, raw reagent ammonium vanadate was reduction in hot acidic solvent, leading to heterogeneous nucleation of NVO nucleus on the surface of autoclave inner wall owing to its unsmooth surface. These $(NH_4)_{0.38}V_2O_5$ nucleus may grow into an ultra-long nanoribbon morphology along [001] direction confirmed by the HRTEM image in Fig. 2e. Simultaneously, the as-grown ultra-long NVO nanoribbon would self-knitted along the autoclave inner wall to form a paper-like sample to gain the lowest systematic free energy.

The uniform, porous NVO/CNTs paper should be an ideal binder-free electrode for ZIBs. The electrochemical properties were subsequently measured in a typical coin-type cell with 2.0 M $ZnSO_4$ aqueous solution as electrolyte. Fig. 3a shows the initial three cycles of cyclic voltammograms (CV) plots for the textile electrode within a voltage window of 0.2–1.5 V vs Zn/Zn^{2+} at a scan speed of 0.1 mV·s^{-1}. In the forward scan, a sharp oxidation peak at 1.27 V was detected, demonstrating the electrochemical de-intercalation of Zn^{2+} from the layered NVO framework. In the reverse scan, a series of reduction peaks at 1.02, 0.92 and 0.66 V continued by a smaller peak (1.38 V) suggests the intercalation of Zn^{2+} ions in the cathode. The origin of these reduction peaks could be due to continuous reductions from V^{5+} to lower oxidation states during the electrochemical process. Noticeably, the first cycled CV profile is different from the rest of the cycles in terms of their oxidation peak positions. XRD measurements were carried out to investigate the phase evolution during the first charging process (Fig. S8). The disappearance of some important diffraction peaks of our NVO sample indicates the irreversible structure change during the first charging process, which should be the main reason for the different CV curves and specific capacity between the first cycle and the succedent cycles [54]. Note that the following CV curves after this phase evolution generally delivers satisfying electrochemical reversibility. In order to further clarify the energy storage mechanisms of our NVO/CNTs paper cathode, a comparison experiments using aqueous electrolyte and H$^+$ absent organic electrolyte (0.5 M $ZnSO_4$ in acetonitrile) was conducted. The CV curves of the NVO/CNTs//Zn batteries in these two different electrolytes shows almost the same CV peak positions with a slight peak offset (Fig. S9). This result should provide evidence on the absence of proton intercalation in our NVO/CNTs cathode. The slight peak offset should be ascribed to the relatively sluggish kinetics of zinc-ion in the organic electrolyte compared to that in the aqueous one.

Fig. 3b depicts the characteristic galvanostatic charge/discharge profile of the paper-like electrode in the initial three cycles. The charge/discharge plateaus are completely corresponding to the redox peak position in the CV curve. From the 2nd cycle onward, the discharge/charge curves are in high coincidence with each other, suggesting a reversible and stable electrochemical performance. The rate capability of the NVO/CNTs electrode in the range of 0.2−1.5 V is evaluated at various current densities (0.1−4 A·g^{-1}) (Fig. 3c). The as-grown binder-free electrode shows very high capacity of 460, 379, 330, 281, 256 and 203 mAh g^{-1} at current densities of 0.1, 0.2, 0.5, 1, 2 and 4 A·g^{-1}, respectively. When the current density is decreased back to 0.1 A·g^{-1}, the capacity returns back to 448 mAh·g^{-1}, demonstrating its outstanding capacity retention at both low and high rates. The improved rate-performance was also verified by the comparison with the conventional electrode prepared through slurrying with PVDF or PTFE as binder, respectively (Fig. 3c).

We then paid more attention on its long-term cycle performance. As shown in Fig. 3d, our NVO/CNTs paper cathode delivers outstanding long-term cyclability with an initial specific capacity of 465 mAh·g^{-1} and retained 89.3 % of the initial specific capacity after 500 cycles at the rate of 0.1 A·g^{-1}. More than 80% of its initial capacity still remained at a current density of 2.0 A·g^{-1} (after 500 cycles), suggesting the excellent cycling stability of the NVO/CNTs paper sample. Even at a high current density of 10 A·g^{-1}, the electrode still delivers capacity retentions of above 50% (Fig. S10). When compared with cycle performance of the electrode with PVDF/PTFE as binder, the binder-free NVO/CNTs sample presented an obvious dominance as expected. Equally unsurprisingly, the pure NVO paper control displays rather poor cycling stability, the capacity of which continues to decline drastically due to its intrinsic low electrical conductivity and self-agreegation (Fig. S11).

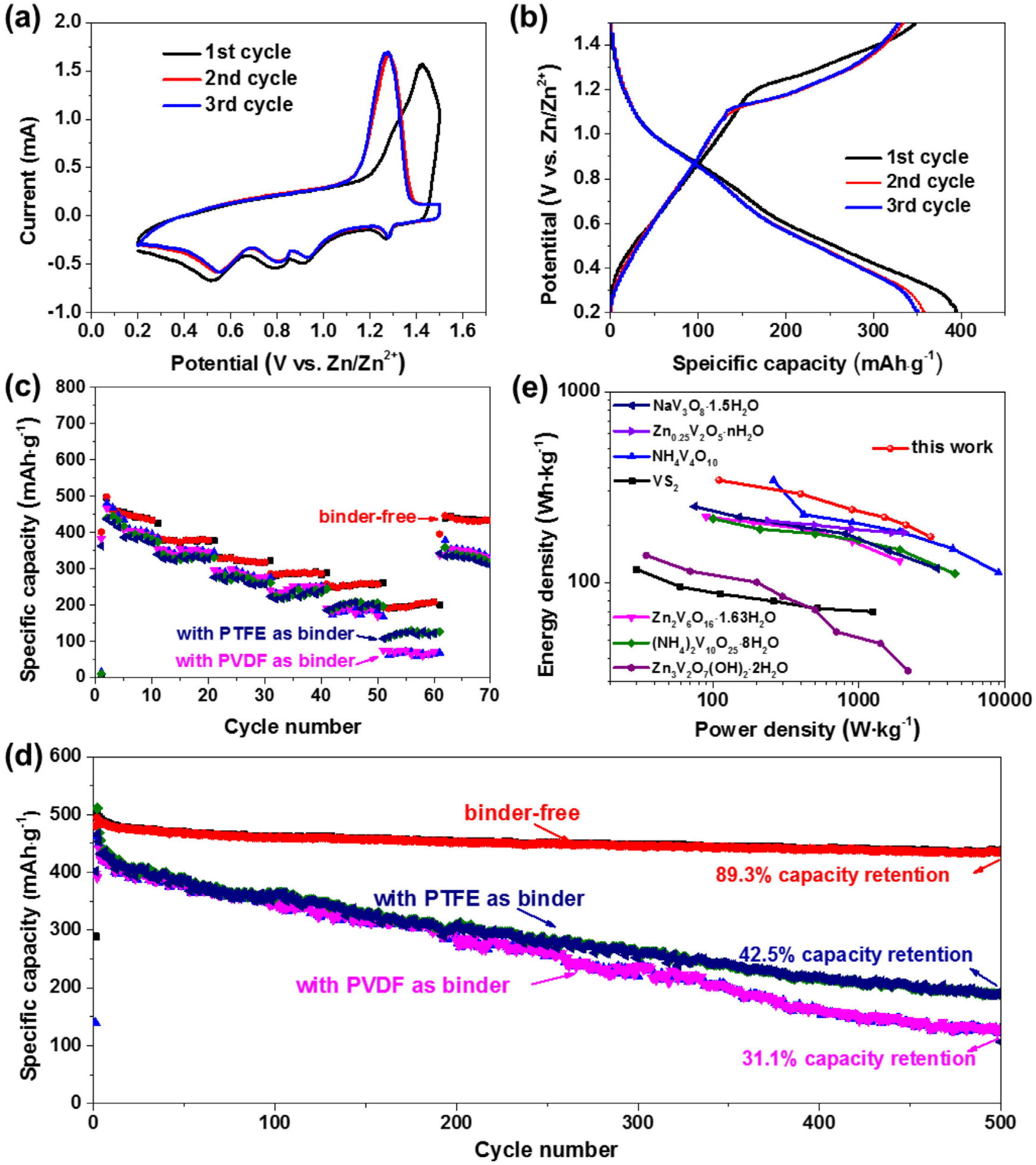

Fig. 3. (a) A representative CV curve of the NVO/CNTs paper electrode for the first to third cycles at a scan rate of 0.1 mV·s^{-1}. (b) Galvanostatic charge–discharge voltage profiles at a current density of 0.4 A·g^{-1}. (c) The rate capability at different current densities of three different electrodes: NVO/CNTs bind-free paper electrode and binder-rich electrodes using PVDF and PTFE respectively (NVO: CNTs: PVDF/PTFE = 8:1:1). PVDF binder based cathode shows inferior rate-performance and capacity retention than that using PTFE binder due to the possible swelling behavior of PVDF in aqueous electrolyte. (d) The cycle performance comparison between the NVO/CNTs paper electrode and the control electrode prepared through slurrying with PVDF/PTFE as binder. (e) Ragone plots of our work compared to other cathodes for aqueous ZIBs.

Additionally, the origin of the extraordinarily high cycling stability in our NVO/CNTs cathode was further identified by the SEM observation of the as-prepared electrode after 100 cycles. As shown in Fig. S12, the 3D network assembled from interconnected 1D nanostructures has been well maintained without obvious structural damage, demonstrating the robust structural stability to endure repeated Zn^{2+} insertion/extraction, leading to superior rate capability and cycling stability.

The superior Zn^{2+} insertion/extraction performance of the NVO/CNTs paper electrode is clearly shown in the Ragone plots by comparison with previously reported cathode materials (based on the active mass of cathodes) for aqueous ZIBs. As presented in Fig. 3e, our electrode achieves the highest specific energy density of 343 Wh·kg^{-1} at a specific power density of 110 W·kg^{-1}, and a decent energy density of 173 Wh·kg^{-1} can be realized with a high specific power density of 3101 W·kg^{-1}. Such an outstanding performance remarkably outperforms most of the ZIBs based on powder form cathode with the presence of polymer binder reported recently including VS_2, [55] $Zn_3V_2O_7(OH)_2{\cdot}H_2O$, [51] $NH_4V_4O_{10}$, [47] $Zn_2V_6O_{16}$, [49] $(NH_4)_2V_{10}O_{25}{\cdot}8H_2O$, [54] $NaV_3O_8{\cdot}1.5H_2O$, [56] $Zn_{0.25}V_2O_5{\cdot}nH_2O$, [57] $ZnMn_2O_4$, [58] Mn_2O_3, [59] $Na_3V_2(PO_4)_2F_3$, [60] ZnHCF, [61] CuHCF, [62] oxygen-deficient V_6O_{13} [63]. Furthermore, the gravimetric energy density of NVO/CNTs//Zn battery based on the active materials in both cathode and anode is 40.94 Wh·kg^{-1}, which is much higher than that of typical commercial supercapacitors (5-10 Wh·kg^{-1}) and comparable to the existing commercial lead-acid batteries (30-40 Wh·kg^{-1}).

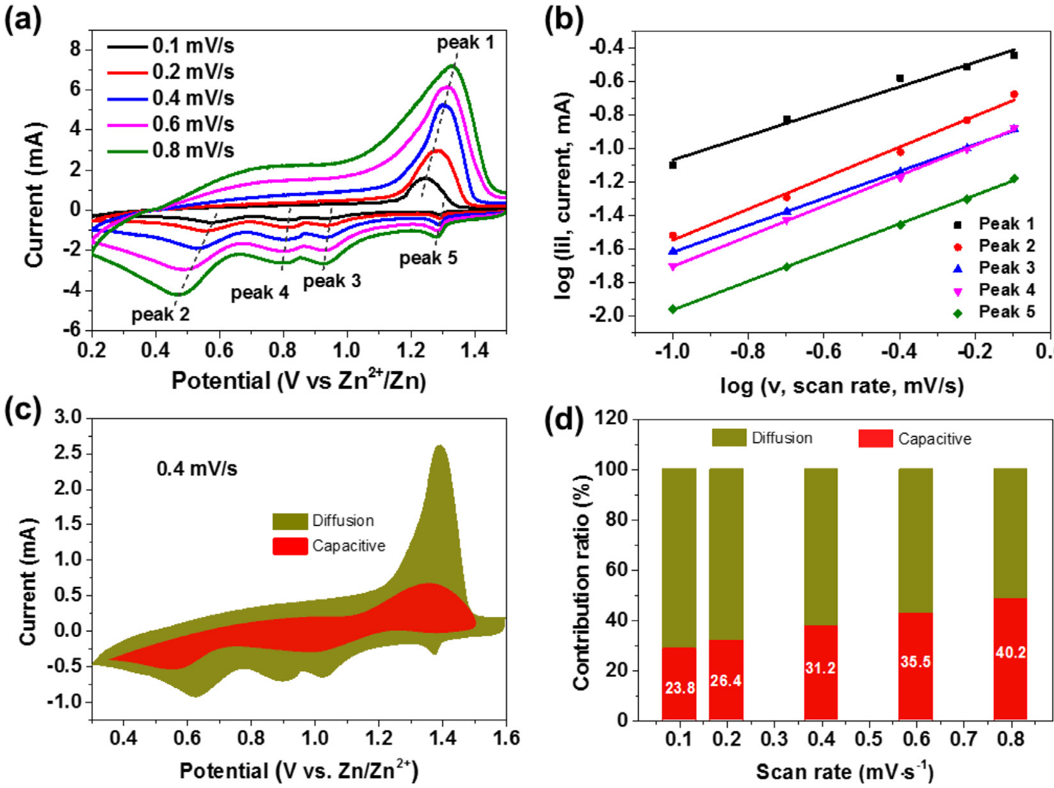

Fig. 4. (a) CV curves of the paper electrode at various sweep rates from 0.1 to 0.8 mV·s^{-1}. (b) The logarithm dependence of peak current density and scan rate in the CV test. (c) The capacitive and diffusion-controlled contribution to the charge storage of NVO/CNTs hybrid film at 0.4 mV·s^{-1}. (d) The normalized contribution ratio of capacitive and diffusion-controlled capacities at different scan rates.

The as-observed excellent Zn^{2+} storage performance should be ascribed to their structural merits in several aspects: (i) The binder-free design guarantees the absence of any organic polymer, and avoids the adsorption between high charge density of Zn^{2+} and the polarizing bonds in the polymeric binder, which significantly facilitates the enhancement on Zn^{2+} mobility during the charge/discharge processes. (ii) The cross-linked networks of flexible NVO nanoribbons and CNTs provide continuous electronic migration pathways in all directions. Other than the conductivity, CNTs in this internal cross-linked structure effectively inhibits the self-aggregation of electrochemical active NVO nanoribbons and prevents mechanical failure upon repeated Zn^{2+} intercalation and ensures long-term durability. (iii) A large number of nanomesh in the 3D network architecture is favorable for the penetration of liquid electrolyte into the whole 3D structure and also for accommodating volume changes upon cycling.

CV scans at different scan rates were conducted to offer further insights into the electrochemical mechanism of Zn^{2+} storage as shown in Fig. 4a. There is almost no distortion of the CV curves as the scan rate increases from 0.1 to 0.8 mV·s^{-1}, further demonstrating its excellent electrochemical stability. We further estimated the pseudocapacitance-like contribution by clarifying the kinetics to separate the capacitive-controlled and diffusion-controlled capacities. The linear relationships of log i vs. log v at the peak potentials are summerized in Fig. 4b. In principle, the peak current (i) is determined by the sweep rate (v) through the following equation:

$$i = av^b \tag{1}$$

$$\log(i) = b \times \log(v) + \log(a) \tag{2}$$

where both a and b represent adjustable parameters. If the b value is 1, the reaction is a capacitor-like process controlled by surface properties, while a b-value of 0.5 corresponds to a process controlled by a semi-infinite linear diffusion [51,64]. The coefficients b of peaks 1, 2, 3, 4 and 5 are determined to be 0.703, 0.901, 0.778, 0.877 and 0.832, respectively, manifesting that the electrochemical reactions are controlled by both capacitor-like process and diffusion controlled intercalation process. Further quantitative analysis has been carried out to investigate the kinetics of the paper electrodes by separating the diffusion controlled capacity and capacitive capacity according to the following equation [65]:

$$i(v) = k_1 v + k_2 v^{1/2} \tag{3}$$

By determining both k_1 and k_2 constants, we can distinguish the fraction of the current from surface capacitance and Zn^{2+} semi-infinite linear diffusion. Fig. 4c shows the capacitive contributions to charge storage in typical CV profile at 0.4 mV·s^{-1}, suggesting the capacitive contribution is more dominant in the total capacity. The contribution ratios for the capacitive current (red region) in comparison with the total current are 23.8%, 26.4%, 31.2%, 35.5% and 40.2% at scan rates of 0.1, 0.2, 0.4, 0.6 and 0.8 mV·s^{-1} (Fig. 4d), respectively, and keeps increasing along with the increase of voltage scan rates. Note that the diffusion controlled intercalation process is more prominent than the capacitive controlled process in our sample, which is presumably due to the aforementioned, large interlayer spacing of layered NVO, which acting as expansive diffusion channel for Zn^{2+} transport.

Finally, we attempted to realize the quasi-solid-state (QSS) ZIBs on a more practical application in the flexible and portable devices as illustrated in Fig. 5a. The quasi-solid-state ZIBs were constructed by employing a ZnSO$_4$/gelatin-based electrolyte, flexible Zn anode, and the as-grown NVO/CNTs paper cathode (Fig. 5b). Compared to a single paper-like ZIB with a charge/discharge potential of 1.3 V, three ZIBs connected in series can achieve 3.9 V and light up a well-designed red light-emitting diode (LED) panel (Fig. 5d). The flexibility of the battery was examined by rolling up the device by hand several times to different bending angles (Fig. 5c), while exhibiting stable discharge ability under

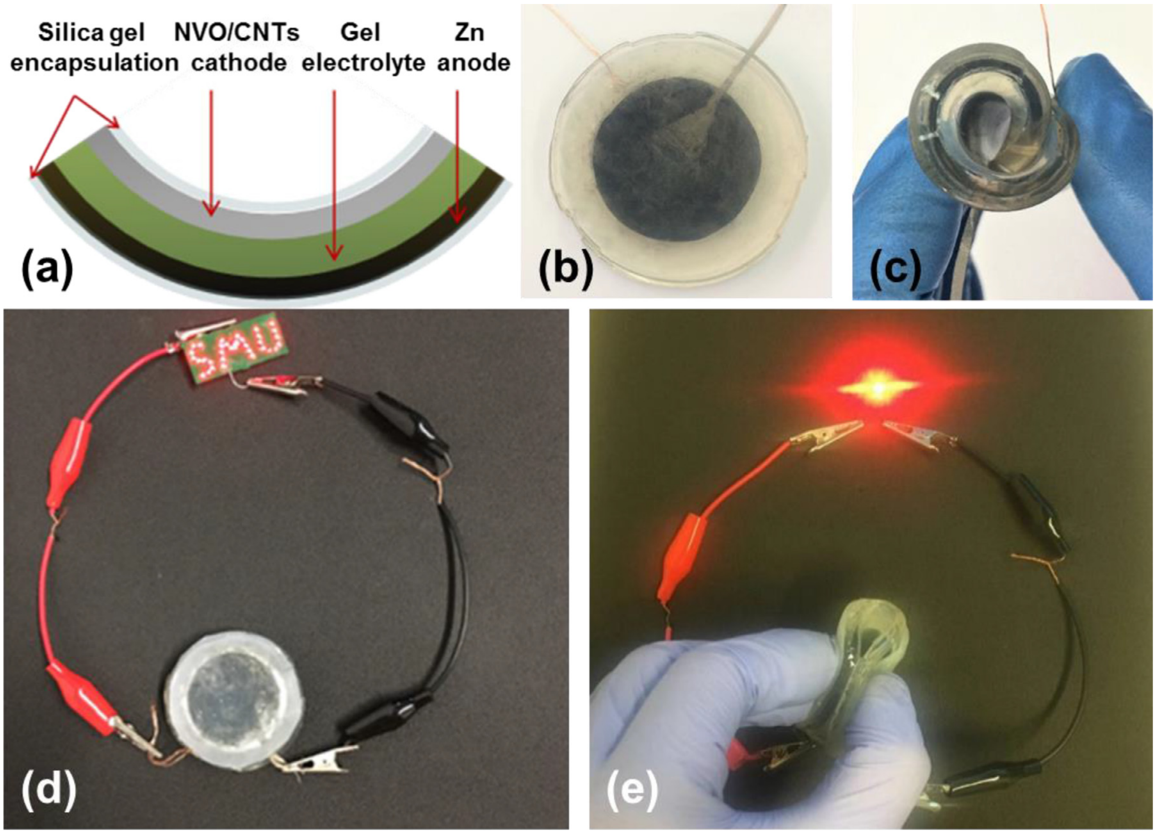

Fig. 5. (a) Schematic illustration of the as-assembled flexible QSS ZIB cell. (b, c) Photograph of the QSS ZIBs and its rolled up state by hand. (d) A LED panel powered by three charged flexible QSS batteries in series. (e) Flexibility and stability of the QSS ZIBs under fully bending states.

fully bending state subjected to continuously mechanical manipulations (Fig. 5e).

3. Conclusion

In summary, we observed a spontaneous knitting behaviour from 6.7 nm thin, flexible NVO nanoribbons in a hydrothermal route to form freestanding paper cathode for aqueous zinc-ion batteries. Optimized by the incorporation of conductive multi-walled carbon nanotubes (CNTs) into this paper-like membrane, the resulting NVO/CNTs hybrid paper delivered a high reversible capacities of 465 mAh·g^{-1} at 100 mA·g^{-1}, and a capacity retention of above 89.3% after 500 cycles at 100 mA·g^{-1} for aqueous Zn^{2+} storage. The energy density of the as-constructed NVO/CNTs//Zn battery was as high as 40.94 Wh·kg^{-1} at a power density of 733.8 W·kg^{-1}. Our work clarify ultrathin NVO nanoribbons is a robust cathode materials for aqueous chargeable ZIBs. More importantly, the observation of their spontaneous knitting behaviour makes a breakthrough on development of binder-free electrode for energy storage application. It would be applicable to the storage of other metal/non-metallic ions (Na^+, Mg^{2+}, Ca^{2+}, Al^{3+}, $NH_4{}^+$ etc.) in next-generation novel batteries.

4. Experimental Section

4.1. Fabrication of freestanding NVO/CNTs composite paper-like electrode

All chemical reagents utilized in this study were of analytical grade and used without further purification. Firstly, CNTs power was were fully dispersed in the deionized water with a concentration of 200 mg/L. In a typical synthesis, 0.575g NH_4VO_3 power (5 mmol) was added into 35 ml deionized water with stirring. Subsequently, the pH value of above solution was adjusted to 6 by dropping diluted hydrochloric acid slowly with continuous stirring. This bright yellow aqueous solution was mixed with 35 mL CNTs dispersion under stirring, then the mixed solution was transferred into a 100 mL Teflon autoclave followed by heating the autoclave in an oven at 190°C for 15 h to allow the formation of NVO/CNTs hybrid film. Upon cooling to room temperature, the grey brown hybrid product like film on the side of the bottle was taken out with caution and was flushed with deionized water and ethanol to compeletely remove residual water-soluble ions, and dried under vacuum at 70 °C for further analysis and application. Without introduction of CNTs, Pure NH_4VO_3 precursor solution with the same concentration and PH as mentioned above still grew into nanowires, and adhered to the wall to aggregate into pure NVO yellow films.

4.2. Fabrication of control electrodes

The control electrode with PVDF(poly(vinylidene) difluoride) as binder was prepared by mixing NVO, CNTs, and PVDF on the basis of a mass ratio of 8:1:1 with the moderate addition of 1-methyl-2-pyrrolidinone; then, the uniform slurry was coated onto a piece of 304 stainless steel foil with thickness of 150 μm and dried at 80°C for 10h in a vacuum oven. The slurry-coated foil cut into electrodes with different shapes served as the cathode (mass loading density: ~2 mg·cm^{-2}). The control electrode with PTFE(polytetrafluorene–ethylene) as binder was prepared by mixing NVO, CNTs, and PTFE on the basis of a mass ratio of 8:1:1 with the moderate addition of isopropyl alcohol as dispersing agent, the rest of the operating process in accordance with the above.

4.3. Battery assembly

The 2032 coin cells were assembled with as-prepared binder-free NVO/CNTs as the cathode, Zinc foil (diameter: 14mm, thickness: 0.01mm, mass: ~10 mg) as anode, glass fiber as separator and 2M $ZnSO_4$

aqueous solution as electrolyte, Such a piece of Φ14 cathode with different thickness ranges in mass from 2.1mg to 3.6mg. A flexible QSS ZIB cell were obtained by pressing a piece NVO/CNTs as the cathode, a zinc foil as the anode, a nonwoven fabric as the separator and the 2M $ZnSO_4$ @ polyvinyl alcohol (PVA) as the electrolyte. The electrolyte was prepared by adding 3 g PVA to 30 mL 2M $ZnSO_4$ aqueous solution little by little with continuous stirring, followed by oil bath treatment at 80 °C for 4h. The ultimate flexible solid-state cell was encapsulated with silicone after the gel electrolyte solidified at room temperature.

4.4. Calculation methods

The specific energy density (Wh·kg^{-1}) and average specific power density (W·kg^{-1}) were calculated in terms of the following equations:

$$E_s = \int_{V_0}^{V_1} C_S(V) \tag{4}$$

$$P_s = \frac{E_s}{t} \tag{5}$$

Where E_s is the calculated specific energy density (Wh·kg^{-1}), P_s is the average specific power density (W·kg^{-1}); C_s (mAh·g^{-1}) is the specific capacity calculated of the battery. V_0 and V_1 is the voltage lower limit and voltage upper limit of discharge procedure, respectively, and t is the discharge time (h). The specific capacity was calculated based on the mass of the active material (NVO) in the electrodes, and the specific energy density and power density were calculated based on the mass of the cathodes. The energy density and power density of the as-constructed NVO/CNTs//Zn battery were calculated based on the total mass of the cell (including both anode and cathode).

4.5. Characterization

The morphologies were observed by scanning electron microscope (SEM, S-4800, Hitachi). The selected area electron diffraction (SAED) pattern and transmission electron microscopy (TEM) images were obtained on a Philips CM200FEG field emission microscope. The crystalline structure was characterized by XRD patterns recorded in a Rigaku D/Max-kA diffractometer with Cu Kα radiation. X-ray photoelectron spectroscopy (XPS, PHI 5000C ESCA System) and Energy dispersive X-ray spectroscopy (EDS, TSL, AMETEK) measurements were employed to investigate the elemental compositions of the samples. The mechanical tests of the resulted papers were performed using a WDW-0.1 electronic universal testing machine (Shanghai Bairoe Test Instrument Co., Ltd).

4.6. Electrochemical measurements

Cyclic voltammetry (CV) curves and electrochemical impedance spectroscopy (100 kHz to 0.1 Hz) were conducted by an electrochemical workstation (CHI 360E). The CV curves of ZIBs were measured based on two-electrode system, in which Zn was used as both counter and reference electrodes (negative electrode) and the composite film NVO/CNTs cathode was used as work electrode (positive electrode). Electrochemical performance of the prepared ZIB was examined based on galvanostatic testing of CR2032-type coin cells (for aqueous ZIBs) and planar thin film battery (for solid-state ZIBs) in the voltage range of 0.2 V - 1.5 V using a Land 2001A battery testing system at 24°C. The area of solid-state ZIB is about 7 cm^2 and the thickness is around 0.11 mm.

Credit Authorship Contribution Statement

Yingchang Jiang: Investigation, Data curation, Writing - original draft. Zeyi Wu: Investigation, Validation, Writing - original draft. Fei Ye: Conceptualization, Writing - original draft. Ruilvjing Pang: Investigation, Data curation. Lin Zhang: Investigation, Data curation. Qiang Liu: Investigation, Writing - original draft. Xueting Chang: Investigation, Project administration. Shibin Sun: Investigation, Project administration. Zhengming Sun: Project administration, Writing - review & editing. Linfeng Hu: Supervision, Project administration, Methodology, Conceptualization, Writing - review & editing.

Declaration of Competing Interest

The authors declare that they have no known competing financial interests or personal relationships that could have appeared to influence the work reported in this paper.

Data availability

Data will be made available on request.

Acknowledgement

This work was financially supported by the National Natural Science Foundation of China (Nos. 51872051, 51731004), the Science and Technology Committee of Shanghai Municipality (18520723100), the Fundamental Research Funds for the Central Universities (2242021R10119), the International Science and Technology Cooperation Program (CU03-29) and the “Shuguang” Program of Shanghai Education Commission (19SG46), Shanghai Engineering Technology research Centre of Deep Offshore Material (19DZ2253100).

Supplementary materials

Supplementary material associated with this article can be found, in the online version, at doi:10.1016/j.ensm.2021.07.045.

References

[1] D.L. Chao, W.H. Zhou, F.X. Xie, C. Ye, H. Li, M. Jaroniec, S.Z. Qiao, Roadmap for advanced aqueous batteries: From design of materials to applications, Sci. Adv. 6 (2020) eaba4098.
[2] G.Z. Fang, J. Zhou, A.Q. Pan, S.Q. Liang, Recent Advances in Aqueous Zinc-ion Batteries, ACS Energy Lett. 3 (10) (2018) 2480–2501.
[3] E.Y. Hu, X.Q. Yang, Rejuvenating zinc batteries, Nat. Mater. 17 (2018) 480–481.
[4] W. Ling, P.P. Wang, Z. Chen, H. Wang, J.Q. Wang, Z.Y. Ji, J.B. Fei, Z.Y. Ma, N. He, Y. Huang, Nanostructure Design Strategies for Aqueous Zinc-Ion Batteries, ChemElectroChem. 14 (2020) 2957–2978.
[5] L.T. Ma, C.Y. Zhi, Zn electrode/electrolyte interfaces of Zn batteries: A mini review, Electrochem. Commun. 122 (2021) 106898.
[6] S. Guo, G.Z. Fang, S.Q. Liang, M.H. Chen, X.W. Wu, J. Zhou, Structural perspective on revealing energy storage behaviors of silver vanadate cathodes in aqueous zinc-ion batteries, Acta Materialia 180 (2019) 51–59.
[7] F. Liu, Z.X. Chen, G.Z. Fang, Z.Q. Wang, Y.S. Cai, B.Y. Tang, J. Zhou, S.Q. Liang, V_2O_5 Nanospheres with Mixed Vanadium Valences as High Electrochemically Active Aqueous Zinc-Ion Battery Cathode, Nano-Micro Lett. 11 (2019) 25.
[8] X.X. Jia, C.F. Liu, Z.G. Neale, J.H. Yang, G.Z. Cao, Active Materials for Aqueous Zinc Ion Batteries: Synthesis, Crystal Structure, Morphology, and Electrochemistry, Chem. Rev. 120 (2020) 7795–7866.
[9] L.Y. Zhang, L. Chen, X.F. Zhou, Z.P. Liu, Towards High-Voltage Aqueous Metal-Ion Batteries Beyond 1.5 V: The Zinc/Zinc Hexacyanoferrate System, Adv. Energy Mater. 5 (2015) 1400930 28.
[10] T. Cao, F. Zhang, M.j. Chen, T. Shao, Z. Li, Q.j. Xu, D.H. Cheng, H.M. Liu, Y.Y. Xia, Cubic Manganese Potassium Hexacyanoferrate Regulated by Controlling of the Water and Defects as a High-Capacity and Stable Cathode Material for Rechargeable Aqueous Zinc-Ion Batteries, ACS Appl. Mater. & Inter. 13 (2021) 26924–26935.
[11] Z. Liu, G. Pulletikurthi, F. Frank Endres, A Prussian Blue/Zinc Secondary Battery with a Bio-Ionic Liquid-Water Mixture as Electrolyte, ACS Appl. Mater. Interfaces 8 (19) (2016) 12158–12164.
[12] B.Q. Wang, Y. Han, X. Wang, N. Bahlawane, H.G. Pan, M. Yan, Y.Z. Jiang, Prussian Blue Analogs for Rechargeable Batteries, iScience 3 (2018) 110–133.
[13] J.Y. Li, L.Y. Li, H.R. Shi, Z.P. Zhong, X.L. Niu, P. Zeng, Z.J. Long, X.Y. Chen, J.; Z. Peng, G. Luo, X.Y. Wang, S.Q. Liang, Electrochemical Energy Storage Behavior of $Na_{0.44}MnO_2$ in Aqueous Zinc-Ion Battery, ACS Sustain. Chem. Eng. 8 (2020) 10673–10681.
[14] N. Zhang, F.Y. Cheng, J.X. Liu, L.B. Wang, X.H. Long, X.S. Liu, F.J. Li, J. Chen, Rechargeable aqueous zinc-manganese dioxide batteries with high energy and power densities, Nat. Commun. 8 (2017) 405.
[15] V. Mathew, B. Sambandam, S. Kim, S. Kim, S. Park, S. Lee, M.H. Alfaruqi, V. Soundharrajan, S. Islam, D.Y. Putro, J.Y. Hwang, Y.K. Sun, J. Kim, Manganese and Vanadium Oxide Cathodes for Aqueous Rechargeable Zinc-Ion Batteries: A Focused View on Performance, Mechanism, and Developments, ACS Energy Lett. 5 (2020) 2376–2400.

[16] M.H. Alfaruqi, V. Mathew, J. Gim, S. Kim, J.J. Song, J.P. Baboo, S.H. Choi, J. Kim, Electrochemically Induced Structural Transformation in a γ-MnO_2 Cathode of a High Capacity Zinc-Ion Battery System, Chem. Mater. 27 (2015) 3609–3620.

[17] H.L. Pan, Y.Y. Shao, P.F. Yan, Y.W. Cheng, K.S. Han, Z.M. Nie, C.M. Wang, J.H. Yang, X.L. Li, P. Bhattacharya, K.T. Mueller, J. Liu, Reversible aqueous zinc/manganese oxide energy storage from conversion reactions, Nat. Energy 1 (2016) 16039.

[18] B.Z. Jiang, C.J. Xu, C.L. Wu, L.B. Dong, J. Li, F.Y. Kang, Manganese Sesquioxide as Cathode Material for Multivalent Zinc Ion Battery with High Capacity and Long Cycle Life, Electrochim. Acta 229 (2017) 422–428.

[19] J.W. Hao, J. Mou, J.W. Zhang, L.B. Dong, W.B. Liu, C.J. Xu, F.Y. Kang, Electrochemically induced spinel-layered phase transition of Mn_3O_4 in high performance neutral aqueous rechargeable zinc battery, Electrochim. Acta 259 (2018) 170–178.

[20] C.Y. Zhu, G.Z. Fang, J. Zhou, J.H. Guo, Z.Q. Wang, C. Wang, J.Y. Li, Y. Tang, S.Q. Liang, Binder-free stainless steel@Mn_3O_4 nanoflower composite: a high-activity aqueous zinc-ion battery cathode with high-capacity and long-cycle-life, J. Mater. Chem. A 6 (2018) 9677–9683.

[21] G.Q. Zhang, T. Wu, H. Zhou, H.R. Jin, K.S. Liu, Y.X. Luo, H.F. Jiang, K. Huang, L. Huang, J. Zhou, Rich Alkali Ions Preintercalated Vanadium Oxides for Durable and Fast Zinc-Ion Storage, ACS Energy Lett. 6 (2021) 2111–2120.

[22] B.Y. Tang, J. Zhou, G.Z Fang, S. Guo, X. Guo, L.T. Shan, Y. Tang, S.Q Liang, Structural Modification of V_2O5 as High-Performance Aqueous Zinc-Ion Battery Cathode, J. Electrochem. Soc. 166 (2019) A480–A486.

[23] N. Bensalah, Y.D. Luna, Recent Progress in Layered Manganese and Vanadium Oxide Cathodes for Zn-Ion Batteries, Energy Tech. 9 (2021) 2100011.

[24] J. Zhou, L.T. Shan, Z.X. Wu, X. Guo, G.Z. Fang, S.Q. Liang, Investigation of V_2O_5 as a low-cost rechargeable aqueous zinc ion battery cathode, Chem. Commun. 54 (2018) 4457–4460.

[25] L.L. Fan, Z.H. Li, N.P. Deng, Recent advances in vanadium-based materials for aqueous metal ion batteries: design of morphology and crystal structure, evolution of mechanisms and electrochemical performance, Energy Storage Mater. 41 (2021) 152–182.

[26] D. Kundu, B.D. Adams, V. Duffort, S.H. Vajargah, L.F. Nazar, A high-capacity and long-life aqueous rechargeable zinc battery using a metal oxide intercalation cathode, Nat. Energy 1 (2016) 16119.

[27] X.M. Xu, F.Y. Xiong, J.S. Meng, X.P. Wang, C.J. Niu, Q.Y. An, L.Q. Mai, Vanadium-Based Nanomaterials: A Promising Family for Emerging Metal-Ion Batteries, *Adv. Funct. Mater.* 30 (2020) 10.

[28] Y.S. Cai, F. Liu, Z.G. Luo, G.Z. Fang, J. Zhou, A.Q. Pan, S.Q. Liang, Pilotaxitic $Na_{1.1}V_3O_{7.9}$ nanoribbons/graphene as high-performance sodium ion battery and aqueous zinc ion battery cathode, Energy Storage Mater. 13 (2018) 168–174.

[29] W.L. Wu, H.Y. Shi, Z.R. Lin, X.P. Yang, C.C. Li, L. Lin, Y. Song, D. Guo, X.X. Liu, X.Q. Sun, The controlled quinone introduction and conformation modification of polyaniline cathode materials for rechargeable aqueous zinc-polymer batteries, Chem.Eng. J. 419 (2021) 129659.

[30] G.L. Li, Z. Yang, Y. Jiang, C.H. Jin, W. Huang, X.L. Ding, Y.H. Huang, Towards polyvalent ion batteries: A zinc-ion battery based on NASICON structured $Na_3V_2(PO_4)_3$, Nano Energy 25 (2016) 211–217.

[31] W. Li, K.L. Wang, S.J. Cheng, K. Jiang, A long-life aqueous Zn-ion battery based on $Na_3V_2(PO_4)_2F_3$ cathode, Energy Storage Mater. 15 (2018) 14–21.

[32] J.Y. Zhu, T.Z. Jian, Y.X. Wu, W.Q. Ma, Y. Lu, L.C. Sun, F.H. Meng, B. Wang, F.P. Cai, J.H. Gao, G.D. Li, L.S. Yang, X.L. Yan, C.X. Xu, A highly stable aqueous Zn/VS_2 battery based on an intercalation reaction, Appl. Surface Sci. 544 (2021) 148882.

[33] E. Madej, M. Espig, R.R. Baumann, W. Schuhmann, E.L. Mantia, Optimization of primary printed batteries based on Zn/MnO_2, J. Power Sources 261 (2014) 356–362.

[34] L.N. Chen, M.Y. Yan, Z.W. Mei, L.Q. Mai, Research progress and prospect of aqueous zinc ion battery, J. Inorg. Mater. 32 (2017) 225–234.

[35] D. Kundu, B.D. Adams, V. Duffort, S.H. Vajargah, L.F. Nazar, A high-capacity and long-life aqueous rechargeable zinc battery using a metal oxide intercalation cathode, Nat. Energy 1 (2016) 16119.

[36] X.D. Hong, B.B. Zhang, E. Murphy, J.L. Zou, F. Kim, Three-dimensional reduced graphene oxide/polyaniline nanocomposite film prepared by diffusion driven layer-by-layer assembly for high-performance supercapacitors, J. Power Sources 343 (2017) 60–66.

[37] B.S. Yin, S.W. Zhang, K. Ke, T. Xiong, Y.M. Wang, B.K.D. Lim, W.S.V. Lee, Z.B. Wang, J.M. Xue, Binder-free V_2O_5/CNT paper electrode for high rate performance zinc ion battery, Nanoscale 11 (2019) 19723–19728.

[38] Y.C. Bai, H. Zhang, B. Xiang, X.Y. Liang, J.Y. Hao, C. Zhu, L.J. Yan, Selenium Defect Boosted Electrochemical Performance of Binder-Free VSe_2 Nanosheets for Aqueous Zinc-Ion Batteries, ACS Appl. Mater. & Inter. 13 (2021) 23230–23238.

[39] Z.Y. Wu, L. Jiang, W.C. Tian, Y.N. Wang, Y.C. Jiang, Q.F. Gu, L.F. Hu, Novel Sub-5 nm Layered Niobium Phosphate Nanosheets for High-Voltage, Cation-Intercalation Typed Electrochemical Energy Storage in Wearable Pseudocapacitors, Adv. Energy Mater. 9 (2019) 1900111.

[40] P.Y. Yang, Z.Y. Wu, Y.C. Jiang, Z.C. Pan, W.C. Tian, L. Jiang, L.F. Hu, Fractal $(NixCo_{1-x})_9Se_8$ Nanodendrite Arrays with Highly Exposed (011) Surface for Wearable, All-Solid-State Supercapacitor, Adv. Energy Mater. 8 (2018) 1801392.

[41] W.T. Dong, M Du, F. Zhang, X.F. Zhang, Z.Y. Miao, H.Z. Li, Y.H. Sang, J.J. Wang, H. Liu, S.H. Wang., Situ Electrochemical Transformation Reaction of Ammonium-Anchored Heptavanadate Cathode for Long-Life Aqueous Zinc-Ion Batteries, ACS Appl. Mater. & Inter. 13 (2021) 5034–5043.

[42] Y.C. Jiang, L. Jiang, Z.Y. Wu, P.Y. Yang, H.T. Zhang, Z.C. Pan, L.F. Hu, In situ growth of $(NH_4)_2V_{10}O_{25}\cdot 8H_2O$ urchin-like hierarchical arrays as superior electrodes for all-solid-state supercapacitors, J. Mater. Chem. A 6 (2018) 16308–16315.

[43] X.B. Yan, J.T. Chen, J. Yang, Q.J. Xue, P. Miele, Fabrication of Freestanding, Electrochemically Active, and Biocompatible Graphene Oxide-Polyaniline and Graphene-Polyaniline Hybrid Papers, ACS Appl. Mater. Inter. 2 (2010) 2521–2529.

[44] X. Liu, G.B. Xu, S.J. Huang, L. Li, Y. Wang, L.W. Yang, Free-standing composite of $Na_xV_2O_5\cdot nH_2O$ nanobelts and carbon nanotubes with interwoven architecture for large areal capacity and high-rate capability aqueous zinc ion batteries, Electrochimica Acta 368 (2021) 137600.

[45] C.N. Yeh, K. Raidongia, J.J. Shao, Q.H. Yang, J.X. Huang, On the origin of the stability of graphene oxide membranes in water, Nat. Chem. 7 (2015) 166–170.

[46] J.W. Lai, H. Tang, X.P. Zhu, Y. Wang, A hydrated $NH_4V_3O_8$ nanobelt electrode for superior aqueous and quasi-solid-state zinc ion batteries, J. Mater. Chem. A 7 (2019) 23140–23148.

[47] B.Y. Tang, J. Zhou, G.Z. Fang, F. Liu, C.Y. Zhu, C. Wang, A.Q. Pan, S.Q. Liang, Engineering the interplanar spacing of ammonium vanadates as a high-performance aqueous zinc-ion battery cathode, J. Mater. Chem. A. 7 (2019) 940–945.

[48] S. Islam, M.H. Alfaruqi, D.Y. Putro, V. Soundharrajan, B. Sambandam, J. Jo, S. Park, S. Lee, V. Mathew, J. Kim, K^+ intercalated V_2O_5 nanorods with exposed facets as advanced cathodes for high energy and high rate zinc-ion batteries, J. Mater. Chem. A 7 (2019) 20335–20347.

[49] V. Soundharrajan, B. Sambandam, S. Kim, M.H. Alfaruqi, D.Y. Putro, J. Jo, S. Kim, V. Mathew, Y.K. Sun, J. Kim, $Na_2V_6O_{16}\cdot 3H_2O$ Barnesite Nanorod: An Open Door to Display a Stable and High Energy for Aqueous Rechargeable Zn-Ion Batteries as Cathodes, Nano Letts. 18 (2018) 2402–2426.

[50] C. Xia, J. Guo, P. Li, X.X. Zhang, H.N. Alshareef, Highly Stable Aqueous Zinc-Ion Storage Using a Layered Calcium Vanadium Oxide Bronze Cathode, Angew. Chem. Int. Ed. 57 (2018) 3943–3949.

[51] C. Xia, J. Guo, Y.J. Lei, H.F. Liang, C. Zhao, H.N. Alshareef, Rechargeable Aqueous Zinc-Ion Battery Based on Porous Framework Zinc Pyrovanadate Intercalation Cathode, Adv. Mater. 30 (2018) 1705580.

[52] Y.L. Zhao, C.H. Han, J.W. Yang, J. Su, X.M. Xu, S. Li, L. Xu, R.P;. Fang, H. Jiang, X.D. Zou, Stable Alkali Metal Ion Intercalation Compounds as Optimized Metal Oxide Nanowire Cathodes for Lithium Batteries, Nano Letts. 15 (2015) 2180–2185.

[53] J. Lee, A. Urban, X. Li, D. Su, G. Hautier, G. Ceder, Unlocking the Potential of Cation-Disordered Oxides for Rechargeable Lithium Batteries, Science 343 (2014) 519–522.

[54] T.Y. Wei, Q. Li, G.Z. Yang, C.X. Wang, Highly reversible and long-life cycling aqueous zinc-ion battery based on ultrathin $(NH_4)_2V_{10}O_{25}\cdot 8H_2O$ nanobelts, J. Mater. Chem. A 6 (2018) 20402–20410.

[55] P. He, M.Y. Yan, G.B. Zhang, R.M. Sun, L.N. Chen, Q.Y. An, L.Q Mai, Layered VS_2 Nanosheet-Based Aqueous Zn Ion Battery Cathode, Adv. Energy Mater. 7 (2017) 1601920.

[56] F. Wan, L.L. Zhang, X. Dai, X.Y. Wang, Z.Q. Niu, J. Chen, Aqueous rechargeable zinc/sodium vanadate batteries with enhanced performance from simultaneous insertion of dual carriers, Nat. Commun. 9 (2018) 1656.

[57] D. Kundu, B.D. Adams, V. Duffort, S.H. Vajargah, L.F. Nazar, A High-Capacity and Long-life Aqueous Rechargeable Zinc Battery Using A Metal Oxide Intercalation Cathode, Nat. Energy 1 (2016) 16119.

[58] N. Zhang, F.Y. Cheng, Y.C. Liu, Q. Zhao, K.X. Lei, C.C. Chen, X.S. Liu, J. Chen, Cation-Deficient Spinel $ZnMn_2O_4$ Cathode in $Zn(CF_3SO_3)_2$ Electrolyte for Rechargeable Aqueous Zn-Ion Battery, J. Am. Chem. Soc. 138 (2016) 12894–12901.

[59] B. Zheng, J. Cheng, J. Xua, C. Wu, L.B. Dong, J. Li, F.Y. Kang, Manganese Sesquioxide as Cathode Material for Multivalent Zinc Ion Battery with High Capacity and Long Cycle Life, Electrochimica Acta 229 (2017) 422–428.

[60] W. Li, K.L. Wang, S.J. Cheng, K. Jiang, A long-life aqueous Zn-ion battery based on $Na_3V_2(PO_4)_2F_3$ cathode, Energy Storage Mater. 15 (2018) 14–21.

[61] L.Y. Zhang, L. Chen, X.F. Zhou, Z.P. Liu, Towards High-Voltage Aqueous Metal-Ion Batteries Beyond 1.5 V: The Zinc/Zinc Hexacyanoferrate System, Adv. energy mater. 5 (2015) 1400930.

[62] R. TrócolI, F.L. Mantia, An Aqueous Zinc-Ion Battery Based on Copper Hexacyanoferrate, ChemSusChem 8 (2015) 481–485.

[63] M. Liao, J.W. Wang, L. Ye, H. Sun, Y.Z. Wen, C. Wang, X.M. Sun, B.J. Wang, H.S. Peng, A Deep-Cycle Aqueous Zinc-Ion Battery Containing an Oxygen-Deficient Vanadium Oxide Cathode, Angew. Chem. Int. Ed. 59 (2020) 2273–2298.

[64] B.Y. Tang, G.Z. Fang, J. Zhou, L.B. Wang, Y.P. Lei, C. Wang, T.Q. Lin, Y. Tang, S.Q. Liang, Potassium vanadates with stable structure and fast ion diffusion channel as cathode for rechargeable aqueous zinc-ion batteries, Nano Energy 51 (2018) 579–587.

[65] Y. Liu, Y.R. Zhou, J.X. Zhang, S.M. Zhang, P. Ren, The relation between the structure and electrochemical performance of sodiated iron phosphate in sodium-ion batteries, Power Sources. 314 (2016) 1–9.